Proceedings of the ASME 2015 International Design Engineering Technical Conferences & Computers and Information in Engineering Conference
IDETC/CIE 2015
August 2-5, 2015, Boston, Massachusetts, USA

DETC2015-46655

STATIC MODELING OF A MULTI-SEGMENT SERPENTINE ROBOTIC TAIL

William S. Rone
Robotics and Mechatronics Laboratory
The George Washington University
Washington, DC, USA

Pinhas Ben-Tzvi
Robotics and Mechatronics Laboratory
The George Washington University
Washington, DC, USA

ABSTRACT

This paper presents a generalized method of determining the static shape conformation of a cable-driven serpentine robot. Given a set of desired cable displacements as model inputs, the model calculates the joint angles and cable tensions that result from those displacements. The model's governing equations are derived from ensuring static equilibrium at each of the robot's revolute joints, along with compatibility equations ensuring the joint angles result in the desired cable displacements. Elastic, actuation and gravitational loading are included in the model, and the results analyze the relative impact of each for various combinations of cable displacement inputs. In addition, the impact of elasticity and mass distribution on the accuracy of purely kinematic constant-curvature segment models is presented. In addition, the model also accommodates limits for the serpentine joint angles. The model is implemented in MATLAB, and results are generated to analyze the impact of the actuation, elastic and gravitational effects. Future work will include inertial effects in the model to make it dynamic. These models will be used as the foundation for a serpentine tail design for use on-board a mobile robot, and for task planning to enable that tail to be effectively used in various scenarios.

1 INTRODUCTION

In nature, tails are observed in numerous species of animals capable of performing a variety of functions. For example, cats use their tails to help balance, monkeys use their tails to help climb, cheetahs use their tails to help turn while running, fish and snakes use their tails for propulsion, kangaroos use their tails as an active counterbalance while jumping, and geckos use their tail's to re-orient while jumping.

As a result, researchers have worked to adapt these biological structures into bioinspired robotic systems and functionalities. Examples include biomimetic fish [1], snakes [2], kangaroos [3], jumping insects [4], terrestrial insects [5], dinosaurs [6], cheetah turning [7] and cheetah acceleration/deceleration [8].

A key application of interest is how ground-based animals use their tails to aid in locomotion—specifically, maneuvering and stabilization. By using a tail to aid in these functionalities on-board a legged robot, the burden on the legs to simultaneously propel, maneuver and stabilize the robot would be reduced. Simplifications to the leg's controlling algorithms would result, along with possible simplifications to the leg structures themselves.

In this work, a two-segment serpentine robotic structure is chosen to implement the robotic tail for a variety of reasons: (1) to enable spatial tail motion, as opposed to the planar motion of a fixed single degree-of-freedom (DOF) pendulum; (2) to enable multiple tail mode shapes, as opposed to uniform bending in a single-segment hyperredundant structure; (3) to preserve a rigid-link structure to simplify modeling and future implementation of the design, as opposed to a continuum structure.

In order to design a serpentine tail capable of generating the required loading to maneuver and stabilize a mobile robot, an accurate numerical model of the serpentine robot is needed. As a first step in this process, a static model is derived capable of calculating the resulting shape of a serpentine robot, as well as tensions within its actuating cables, based on the prescribed actuation cable displacements. Previous work in cable-driven robotics [9,10] has focused on utilizing these models primarily to predict the spatial shape of the robot, whereas this research focuses primarily on the dynamic loading generated by these systems.

The paper is organized as follows: Section 2 presents background research in the fields of serpentine robotics and ground-based mobile robotic tails. Section 3 presents the design concept for the robotic tail, along with the two analytical models: a uniform-curvature kinematic model and a statics model. Section 4 discusses the numerical

implementation of the kinematic and statics models in MATLAB. Section 5 analyzes the impact of actuation, elastic and gravitational loading on the accuracy of the purely kinematic model

2 BACKGROUND

This section presents the previous research in the topics of serpentine robots and robotic tails.

2.1 Serpentine Robots

Serpentine robots are rigid-link robotic systems that are composed of a large number of distinct rigid-bodies (often identical) capable of bending in what appear to be continuous curves. They are distinguished from conventional rigid-link robots by the large numbers of DOFs, as well as the uniformity between the rigid bodies. They are distinguished from continuum robots by the lack of continuous elastic backbone.

The primary application studied in the literature related to serpentine robots is snake-like locomotion [2,11,12]. In most of these structures, actuation is distributed along the length of the robot within each module, and each joint is individually actuated to enable terrestrial locomotion or climbing. In a tail-like structure, this actuation structure is undesirable, because individual joint actuation is not a requirement, and the distribution of actuators along the robot will mandate an increase in the tail's mass (as opposed to letting it remain a design variable).

Medical applications, including diagnosis and surgery, have also been addressed using serpentine robots [13,14]. However, these robots operate on the meso-scale, in which elastic effects dominate in comparison to dynamic and gravitational effects, compared to the macro-scale tails under consideration in this paper.

Serpentine robots have also been used in industrial applications for inspection of systems ranging from nuclear facilities to airplanes [15]. The design concept presented is similar to the design analyzed in this paper, with similar rigid links joined together by universal joints and actuated by cabling. However, these types of robots are designed to be fairly rigid, to minimize the impact of external loading on their shape during operation. The tail will need to be more agile, particularly toward the tip, to enable rapid dynamic motions to generate the required inertial loading.

2.2 Ground Mobile Robotic Tails

Previous research associated with mimicking biological tails on robots has focused on one- or two-DOF rigid-link pendulums [3–8,16,17]. In each case, the tail is designed to perform a specific function: yaw-angle steering [5,7,16], pitch angle modification [3,4], center-of-mass (COM) positioning [6], aiding in accelerating/decelerating [8] and propulsion [17].

However, in each case, the tail was designed to only perform a single function. In an actual system, though, it would be desirable for a tail to be able to perform several of these functions in a single structure. The spatial serpentine tail analyzed in this paper is capable of this desired multifunctional operation.

3 TAIL DESIGN AND MATHEMATICAL MODEL

This section presents the design concept for the serpentine tail, and two mathematical models for representing the serpentine tail: a uniform-curvature kinematic model, and a statics model.

3.1 Design Concept

Figure 1 shows an illustration of the serpentine tail design under consideration. The tail is composed of six universal joints along its links, with disks mounted between the joints and at the end of the tail to help route cabling. Six cables are used to actuate the robot: three defining segment 1, which terminate at the disk 3; and three defining segment 2, which terminate at disk 6. The actuation for the six cables is contained within the actuation module at the base of the tail, and this actuation module will be what is attached to a legged prototype in future work.

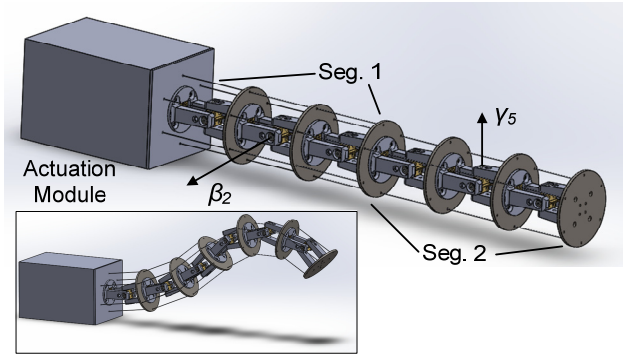

Figure 1. Two-segment serpentine tail.

Figure 2 shows a single subsegment between two disks. The two "halves" of the universal joint connect to the disks on either side, and are both connected by revolute joints to the universal joint "center" in the middle. The universal joint halves are rotated 90° with respect to one another to create the two orthogonal revolute joints defining the universal joint.

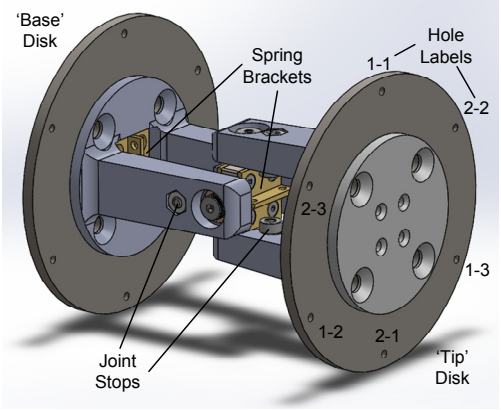

Figure 2. Serpentine tail subsegment.

In each subsegment i, the universal joint is oriented so that the first joint in the universal joint controls the vertical rotation (i.e., y-axis rotation, defined by the angle β_i) and the second joint controls the horizontal motion (i.e., x-axis rotation, defined by the angle γ_i). However, if $\beta_i \neq 0$, the x-axis will not align with the x-axis at the base of the subsegment.

For this tail, it is desirable to have $\pm 90^o$ range for each segment bending, so the joint angle range for each joint is set to $\pm 35^o$ (to accommodate possible overshoot during dynamic motions studied in future analyses).

Two pairs of antagonistic extension springs are used to create the elastic loading in the two orthogonal joints. When $\beta_i = \gamma_i = 0$, the joints are equally pre-tensioned to result in a net zero elastic moment on each joint. When the joint displaces, the moment increases along a linear profile within the $[-35^o, 35^o]$ joint angle range.

3.2 Tail Kinematics

For each subsegment i, there are two key frames of reference needed for subsequent calculations: the joint center frame $\boldsymbol{R}_{jnt,i}$ and the disk frame $\boldsymbol{R}_{dsk,i}$. These frames are calculated by first calculating the local frames within each subsegment, then recursively calculating the frames from the base to the tip. Equation (1) shows the calculation of the local frames $\boldsymbol{R}_{jnt,i,lcl}$ and $\boldsymbol{R}_{dsk,i,lcl}$, and Eq. (2) shows the recursive calculation of the global frames $\boldsymbol{R}_{jnt,i}$ and $\boldsymbol{R}_{dsk,i}$.

$$\boldsymbol{R}_{jnt,i,lcl} = \begin{bmatrix} c_{\beta,i} & 0 & s_{\gamma,i} \\ 0 & 1 & 0 \\ -s_{\gamma,i} & 0 & c_{\beta,i} \end{bmatrix}, \quad \boldsymbol{R}_{dsk,i,lcl} = \boldsymbol{R}_{jnt,i,lcl} \begin{bmatrix} 1 & 0 & 0 \\ 0 & c_{\gamma,i} & -s_{\gamma,i} \\ 0 & s_{\gamma,i} & c_{\gamma,i} \end{bmatrix} \tag{1}$$

$$\boldsymbol{R}_{jnt,i} = \begin{cases} \boldsymbol{R}_{jnt,i,lcl} & i = 1 \\ \boldsymbol{R}_{dsk,i-1}\boldsymbol{R}_{jnt,i,lcl} & i > 1 \end{cases}, \quad \boldsymbol{R}_{dsk,i} = \begin{cases} \boldsymbol{R}_{dsk,i,lcl} & i = 1 \\ \boldsymbol{R}_{dsk,i-1}\boldsymbol{R}_{dsk,i,lcl} & i > 1 \end{cases} \tag{2}$$

Using these rotation matrices, the centroid positions of the joint centers $\boldsymbol{p}_{jnt,i}$ and disks $\boldsymbol{p}_{dsk,i}$ can be calculated using Eq. (3):

$$\boldsymbol{p}_{jnt,i} = \begin{cases} \begin{bmatrix} 0, & 0, & L_{dsk2jnt} \end{bmatrix}^T & i = 1 \\ \boldsymbol{p}_{dsk,i-1} + \boldsymbol{R}_{dsk,i-1} \begin{bmatrix} 0, & 0, & L_{dsk2jnt} \end{bmatrix}^T & i > 1 \end{cases} \tag{3}$$

$$\boldsymbol{p}_{dsk,i} = \boldsymbol{p}_{jnt,i} + \boldsymbol{R}_{dsk,i} \begin{bmatrix} 0, & 0, & L_{jnt2dsk} \end{bmatrix}^T$$

where $L_{dsk2jnt}$ is the distance from the subsegment's 'base' disk to the joint center, and $L_{jnt2dsk}$ is the distance from the joint center to the subsegment's 'tip' disk.

In order to define the tail kinematic model governing equations, calculations for the actuation cable lengths $L_{cbl,j,k}$ for cable k terminating in segment j are needed.

Because they terminate in different segments, each cable does not necessarily pass through all six subsegments. The cables terminating in segment 1 only pass through subsegments 1-3, whereas the cables terminating in segment 2 pass through subsegments 1-6. In the following derivations, the subsegment index i will iterate from 1:3 if the segment index $j = 1$, or will iterate from 1:6 if the segment index $j = 2$.

The local position $\boldsymbol{p}_{hl,j,k,lcl}$ of each routing hole depends on the segment j in which the cable terminates and the specific cable k terminating there. In Fig. 2, the holes in the 'tip' disk are labeled j-k, corresponding to the specific cable that passes through that hole. Equation (4) defines the coordinates mathematically, where r_h is the cable routing hole radius.

$$\begin{aligned} \theta_{j,k} &= (j-1)*180^o + (k-1)*120^o \\ \boldsymbol{p}_{hl,j,k,lcl} &= r_h \begin{bmatrix} \cos(\theta_{j,k}) & \sin(\theta_{j,k}) & 0 \end{bmatrix}^T \end{aligned} \tag{4}$$

The position $\boldsymbol{p}_{hl,i,j,k}$ relative to the base frame of the segment j, cable k routing hole in disk i, is calculated using Eq. (5):

$$\boldsymbol{p}_{hl,i,j,k} = \boldsymbol{p}_{dsk,i} + \boldsymbol{R}_{dsk,i}\boldsymbol{p}_{hl,j,k,lcl} \tag{5}$$

Using $\boldsymbol{p}_{hl,i,j,k}$, the hole-to-hole position vectors $\boldsymbol{p}_{h2h,i,j,k}$ are calculated using Eq. (6), with a slight modification for the first subsegment, given that the actuation module precedes it:

$$\boldsymbol{p}_{h2h,i,j,k} = \begin{cases} \boldsymbol{p}_{hl,i,j,k} - \boldsymbol{p}_{hl,j,k,lcl} & i = 1 \\ \boldsymbol{p}_{hl,i,j,k} - \boldsymbol{p}_{hl,i-1,j,k} & i > 1 \end{cases} \tag{6}$$

The subsegment cable lengths $L_{h2h,i,j,k}$ are the magnitudes of $\boldsymbol{p}_{h2h,i,j,k}$, as shown in Eq. (7), and the summation of these subsegment lengths for the corresponding number of subsegments (3 when $j = 1$, or 6 when $j = 2$) is the total actuation cable length $L_{cbl,j,k}$ in the given configuration, as shown in Eq. (8).

$$L_{h2h,i,j,k} = \left| \boldsymbol{p}_{h2h,i,j,k} \right| \tag{7}$$

$$L_{cbl,j,k} = \begin{cases} \sum_{i=1}^{3} L_{h2h,i,j,k} & j = 1 \\ \sum_{i=1}^{6} L_{h2h,i,j,k} & j = 2 \end{cases} \tag{8}$$

3.3 Tail Kinematic Model Governing Equations

The key simplifying assumption for the purely kinematic model is that in each segment, the three β_i angles are equal and the three γ_i angles are each equal, ensuring uniform bending along each segment defining the tail. As a result, the model can be defined by four DOFs: $\beta_A, \beta_B, \gamma_A$ and γ_B, where $\beta_A = \beta_1 = \beta_2 = \beta_3$, $\beta_B = \beta_4 = \beta_5 = \beta_6$, $\gamma_A = \gamma_1 = \gamma_2 = \gamma_3$ and $\gamma_B = \gamma_4 = \gamma_5 = \gamma_6$.

The four governing equations for the model derive from specifying two desired actuation cable lengths $L_{cbl,j,k,des}$ for the triplet of cables terminating in each segment. For example, in segment 1, the lengths of cables 1 and 2, 2 and 3, or 3 and 1 can be specified. Conventionally, the cables for which the displacements are specified will be the cables in tension. However, neither model requires this. Equation (9) mathematically defines the four governing equations for the model. The choice of form for these governing equations is to aid in numerical implementation in Section 4.

$$\begin{cases} L_{cbl,1,k,des} - L_{cbl,1,k} = 0 & k = \{[1,2],[2,3],[3,1]\} \\ L_{cbl,2,k,des} - L_{cbl,2,k} = 0 & k = \{[1,2],[2,3],[3,1]\} \end{cases} \tag{9}$$

3.4 Tail Statics Model Governing Equations

For the two-segment, six subsegment tail shown in Fig. 1, there are 16 DOF: six β_i angles, six γ_i angles, and four cable tensions. Therefore, 16 governing equations are needed.

Twelve of the governing equations will be static equilibrium equations at each of the 12 joints along the robot. By definition, in static equilibrium, a revolute joint cannot support a moment aligned with its axis of rotation. Therefore, the dot product between the internal moment $\boldsymbol{M}_{int,i,h}$ at the joint and the joint's axis of rotation should be zero, as shown in Eq. (10). The subscript h corresponds to either the β joint ($h = 1$) or the γ joint ($h = 2$).

$$\begin{cases} \left|M_{net,i,1}\right| = \boldsymbol{M}_{int,i,1} \cdot \boldsymbol{R}_{jnt,i} \begin{bmatrix} 0 & 1 & 0 \end{bmatrix}^T = 0 \\ \left|M_{net,i,2}\right| = \boldsymbol{M}_{int,i,2} \cdot \boldsymbol{R}_{jnt,i} \begin{bmatrix} 1 & 0 & 0 \end{bmatrix}^T = 0 \end{cases} \tag{10}$$

Section 3.5 describes the recursive calculation of the internal moments (and associated internal forces) from the tip of the tail to the base. Sections 3.6, 3.7 and 3.8 describe the calculations associated with the gravitational, elastic and actuation loading, respectively, that are used to calculate the internal loading.

The other four governing equations will be the cable displacement compatibility equations used in the kinematic model and defined in Eq. (8). In the kinematic model, those equations are used to calculate the four joint angles that define the kinematic configuration of the robot. In the statics model, those equations are used to constrain four of the joint angles so that the static equilibrium equations can also be used to calculate the required actuation loading, and as a result, the cable tensions.

3.5 Internal Loading

The internal loading carried through the robot is the force and moment transmitted from joint-to-joint from the tip of the robot (where the internal loading is zero) to the base. It is calculated recursively beginning at the subsegment 6 ($i = 6$) γ-joint ($h = 2$), moving back to the subsegment 6 β-joint ($h = 1$), then to the subsegment 5 ($i = 5$) γ-joint ($h = 2$), and following the same pattern until the base is reached.

The sum of the forces acting on the disk assembly constitute the internal force $\boldsymbol{F}_{int,i,2}$ for the γ-joint, calculated in Eq. (11), and the sum of the forces acting on the joint center constitute the internal force $\boldsymbol{F}_{int,i,1}$ for the β-joint, calculated in Eq. (12). For all $\boldsymbol{F}_{int,i,h}$ except $\boldsymbol{F}_{int,6,2}$, the subsequent joint's internal forces is included in the internal force calculation, because the effect of the internal force from the tip to the base is cumulative.

$$\boldsymbol{F}_{int,i,2} = \begin{cases} \boldsymbol{F}_{grv,dsk,i} + \boldsymbol{F}_{sp,tot,i,h} + \boldsymbol{F}_{act,tot,i} & i = 6 \\ \boldsymbol{F}_{int,i+1,1} + \boldsymbol{F}_{grv,dsk,i} + \boldsymbol{F}_{sp,tot,i,h} + \boldsymbol{F}_{act,tot,i} & i < 6 \end{cases} \tag{11}$$

$$\boldsymbol{F}_{int,i,1} = \boldsymbol{F}_{int,i,2} + \boldsymbol{F}_{grv,jnt,i} + \boldsymbol{F}_{sp,tot,i,h} \tag{12}$$

Most of the forces will also generate a moment with respect to their associated joints. The exception is $\boldsymbol{F}_{grv,jnt}$ because its point of application lies on the β-joint axis. The resulting internal moments due to these loading effects for the γ-joints ($\boldsymbol{M}_{int,i,2}$) are calculated in Eq. (13), and the internal moments for the β-joints ($\boldsymbol{M}_{int,i,1}$) are calculated in Eq. (14). However, in the computation of these internal moments, three additional terms have been included and will be explained in the following two paragraphs.

$$\boldsymbol{M}_{int,i,2} = \begin{cases} \boldsymbol{M}_{grv,dsk,i} + \boldsymbol{M}_{el,tot,i,2} + \boldsymbol{M}_{act,tot,i} & i = 6 \\ \begin{pmatrix} \boldsymbol{M}_{int,i+1,1} + \boldsymbol{M}_{grv,dsk,i} \\ + \boldsymbol{M}_{el,tot,i,2} + \boldsymbol{M}_{act,tot,i} + \boldsymbol{M}_{F\_int,i} \end{pmatrix} & i < 6 \end{cases} \tag{13}$$

$$\boldsymbol{M}_{int,i,1} = \boldsymbol{M}_{int,i,2} + \boldsymbol{M}_{el,tot,i,2} \tag{14}$$

The final term in the $i < 6$ case of Eq. (13) accounts for the moment generated by the subsequent joint's internal force. It is calculated in Eq. (15).

$$\boldsymbol{M}_{F\_int,i} = \left(\boldsymbol{p}_{jnt,i+1} - \boldsymbol{p}_{jnt,i}\right) \times \boldsymbol{F}_{int,i+1,1} \tag{15}$$

3.6 Gravitational Loading

Along the tail, there are three types of bodies contributing to the gravitational loading: the joint center assemblies (mass: m_{jnt}), the five whole disk-assemblies along the tail (mass: $m_{dsk,whl}$), and the half disk-assembly at the tip of the robot (mass: $m_{dsk,hlf}$). The gravitational forces $\boldsymbol{F}_{grv,jnt,i}$ and $\boldsymbol{F}_{grv,dsk,i}$ associated with these bodies are defined in Eq. (16), where g is gravitational acceleration:

$$\begin{aligned} \boldsymbol{F}_{grv,jnt,i} &= -m_{jnt} g \begin{bmatrix} 1 & 0 & 0 \end{bmatrix}^T \\ \boldsymbol{F}_{grv,dsk,i} &= \begin{cases} -m_{dsk,whl} g \begin{bmatrix} 1 & 0 & 0 \end{bmatrix}^T & i < 6 \\ -m_{dsk,hlf} g \begin{bmatrix} 1 & 0 & 0 \end{bmatrix}^T & i = 6 \end{cases} \end{aligned} \tag{16}$$

However, based on the design of the tail's subsegments, the disk assembly COM may not intersect with the disk center (this is obvious for the half disk-assembly). As a result, the disk COM position $\boldsymbol{p}_{COM,dsk,i}$ should be calculated using Eq. (17), where $L_{COM,dsk,i}$ is the distance from the γ-joint axis of rotation to the disk assembly COM.

$$\boldsymbol{p}_{COM,dsk,i} = \boldsymbol{p}_{jnt,i} + L_{COM,dsk,i} \boldsymbol{R}_{dsk,i} \begin{bmatrix} 0 & 0 & 1 \end{bmatrix}^T \tag{16}$$

Using this COM position, the moment due to $\boldsymbol{F}_{grv,dsk,i}$ can be calculated using Eq. (17).

$$\boldsymbol{M}_{grv,dsk,i} = \left(\boldsymbol{p}_{COM,dsk,i} - \boldsymbol{p}_{jnt,i}\right) \times \boldsymbol{F}_{grv,dsk,i} \tag{17}$$

As discussed in Section 3.5, because the joint center COM intersects the β-joint axis of rotation, there is no moment associated with the joint center weight.

3.7 Elastic Loading

In each subsegment, there are four pairs of spring attachment points. The position vector between each pair in which a spring is mounted defines both the spring force magnitude (based on the spring's displacement from its unloaded position) and direction (based on the position's unit vector).

In order to calculate the displacement between these spring anchor points, their positions need to be defined with respect to the nearest disk or joint center. For a given subsegment i, there are four pairs of anchors along the length of the subsegment. Table 1 describes the four spring attachment point pair displacements $\boldsymbol{p}_{sp,h,n,q,lcl}$, where h is the associated joint, n is the associated spring and q is the first or second attachment point relative to the base. Table 1 also specifies the position to which this local displacement is relative. In each case, when $n = 1$, r_{sp} is positive, and when $n = 2$, r_{sp} is negative.

Table 1. Local spring attachment points

Local Displacement:	Relative To:
$\boldsymbol{p}_{sp,1,n,1,lcl} = \left[\pm r_{sp},\ \ 0,\ \ d_{sp,dsk}\right]^T$	$\boldsymbol{p}_{dsk,i-1}$
$\boldsymbol{p}_{sp,1,n,2,lcl} = \left[\pm r_{sp},\ \ 0,\ \ -d_{sp,jnt}\right]^T$	$\boldsymbol{p}_{jnt,i}$
$\boldsymbol{p}_{sp,2,n,1,lcl} = \left[0,\ \ \pm r_{sp},\ \ d_{sp,jnt}\right]^T$	$\boldsymbol{p}_{jnt,i}$
$\boldsymbol{p}_{sp,2,n,2,lcl} = \left[0,\ \ \pm r_{sp},\ \ d_{sp,dsk}\right]^T$	$\boldsymbol{p}_{dsk,i}$

Using these local displacements, the global spring attachment positions $\boldsymbol{p}_{sp,i,h,n,q}$ can be calculated using Eq. (18).

$$\begin{aligned}
\boldsymbol{p}_{sp,i,1,n,1} &= \begin{cases} \boldsymbol{p}_{sp,1,n,1,lcl} & i = 1 \\ \boldsymbol{p}_{dsk,i-1} + \boldsymbol{R}_{dsk,i-1}\boldsymbol{p}_{sp,1,n,1,lcl} & i > i \end{cases} \\
\boldsymbol{p}_{sp,i,1,n,2} &= \boldsymbol{p}_{jnt,i} + \boldsymbol{R}_{jnt,i}\boldsymbol{p}_{sp,1,n,2,lcl} \\
\boldsymbol{p}_{sp,i,2,n,1} &= \boldsymbol{p}_{jnt,i} + \boldsymbol{R}_{jnt,i}\boldsymbol{p}_{sp,2,n,1,lcl} \\
\boldsymbol{p}_{sp,i,2,n,2} &= \boldsymbol{p}_{dsk,i} + \boldsymbol{R}_{dsk,i}\boldsymbol{p}_{sp,2,n,2,lcl}
\end{aligned} \tag{18}$$

The positon vector for spring n associated with joint h in subsegment i is $\boldsymbol{p}_{sp,i,h,n}$ and is defined in Eq. (19).

$$\boldsymbol{p}_{sp,i,h,n} = \boldsymbol{p}_{sp,i,h,n,2} - \boldsymbol{p}_{sp,i,h,n,1} \tag{19}$$

The spring lengths $L_{sp,i,h,n}$ and unit direction vectors $\hat{\boldsymbol{p}}_{sp,i,h,n}$ are calculated using Eq. (20).

$$L_{sp,i,h,n} = \left|\boldsymbol{p}_{sp,i,h,n}\right|, \quad \hat{\boldsymbol{p}}_{sp,i,h,n} = \boldsymbol{p}_{sp,i,h,n} \big/ L_{sp,i,h,n} \tag{20}$$

The spring force magnitude $F_{sp,i,h,n}$ depends on the displacement of the spring from the unloaded length $L_{sp,0}$, the spring constant $k_{sp,i}$ and the pre-tension $F_{sp,pre,i}$, as shown in Eq. (21).

$$F_{sp,i,h,n} = k_{sp,i}\left(L_{sp,i,h,n} - L_{sp,0}\right) + F_{sp,pre,i} \tag{21}$$

Each side q of spring n associated with joint h in subsegment i will apply a force $\boldsymbol{F}_{el,i,h,n,q}$ to either the disk assembly (when $q = h$) or joint center (when $q \neq h$), as defined in Eq. (22).

$$\boldsymbol{F}_{el,i,h,n,q} = \begin{cases} F_{sp,i,h,n}\hat{\boldsymbol{p}}_{sp,i,h,n} & q = 1 \\ -F_{sp,i,h,n}\hat{\boldsymbol{p}}_{sp,i,h,n} & q = 2 \end{cases} \tag{22}$$

The spring forces when $[h,q] = [1,1]$ and $[2,2]$ will contribute to the total force $\boldsymbol{F}_{el,tot,i,2}$ and moment $\boldsymbol{M}_{el,tot,i,2}$, and the spring forces when $[h,q] = [1,2]$ and $[2,1]$ will contribute to the total force $\boldsymbol{F}_{el,tot,i,1}$ moment $\boldsymbol{M}_{el,tot,i,1}$. Each of these is defined in Eqs. (23) and (24).

$$\begin{aligned}
\boldsymbol{F}_{el,tot,i,1} &= \sum_{n=1}^{2}\left[\boldsymbol{F}_{el,i,1,n,2} + \boldsymbol{F}_{el,i,2,n,1}\right] \\
\boldsymbol{F}_{el,tot,i,2} &= \begin{cases} \sum_{n=1}^{2}\left[\boldsymbol{F}_{el,i,2,n,2} + \boldsymbol{F}_{el,i+1,1,n,1}\right] & i < 6 \\ \sum_{n=1}^{2}\boldsymbol{F}_{el,i,2,n,2} & i = 6 \end{cases}
\end{aligned} \tag{23}$$

$$\begin{aligned}
\boldsymbol{M}_{el,tot,i,1} &= \sum_{n=1}^{2}\begin{bmatrix} \left(\boldsymbol{p}_{sp,i,1,n,2} - \boldsymbol{p}_{jnt,i}\right)\times\boldsymbol{F}_{el,i,1,n,2} \\ +\left(\boldsymbol{p}_{sp,i,2,n,1} - \boldsymbol{p}_{jnt,i}\right)\times\boldsymbol{F}_{el,i,2,n,1} \end{bmatrix} \\
\boldsymbol{M}_{el,tot,i,2} &= \begin{cases} \sum_{n=1}^{2}\begin{bmatrix} \left(\boldsymbol{p}_{sp,i,2,n,2} - \boldsymbol{p}_{jnt,i}\right)\times\boldsymbol{F}_{el,i,2,n,2} \\ +\left(\boldsymbol{p}_{sp,i+1,1,n,1} - \boldsymbol{p}_{jnt,i}\right)\times\boldsymbol{F}_{el,i+1,1,n,1} \end{bmatrix} & i < 6 \\ \sum_{n=1}^{2}\left(\boldsymbol{p}_{sp,i,2,n,2} - \boldsymbol{p}_{jnt,i}\right)\times\boldsymbol{F}_{el,i,2,n,2} & i = 6 \end{cases}
\end{aligned} \tag{24}$$

3.8 Actuation Loading

The actuation loading will be formulated in a similar manner to the cable loading in [18]. Continuing from the analysis in Section 3.2, using the hole-to-hole vectors and subsegment cable lengths, the unit vectors associated with the cable actuation forces can be calculated using Eq. (25).

$$\hat{\boldsymbol{p}}_{h2h,i,j,k} = \boldsymbol{p}_{h2h,i,j,k} \big/ L_{h2h,i,j,k} \tag{25}$$

In the statics model, the four non-zero cable tensions $T_{j,k}$ represent four of the model's DOF. However, during the iterative calculations, the current tension values are available to the solver for use in calculations, similar to how the current joint angles are available for use in calculations. Therefore, the actuation forces $\boldsymbol{F}_{act,i,j,k}$ acting on disk-assembly i from cable j at hole k are defined in Eq. (26). In this model, friction is neglected.

$$\boldsymbol{F}_{act,i,j,k} = \begin{cases} T_{j,k}\left(\hat{\boldsymbol{p}}_{h2h,i+1,j,k} - \hat{\boldsymbol{p}}_{h2h,i,j,k}\right) & i < 3j \\ -T_{j,k}\hat{\boldsymbol{p}}_{h2h,i,j,k} & i = 3j \end{cases} \tag{26}$$

The actuation forces will only explicitly contribute to the internal forces and moments associated with the γ-joint, as shown in Eq. (11) and (13). The resulting calculations for $\boldsymbol{F}_{act,tot,i}$ and $\boldsymbol{M}_{act,tot.i}$ are shown in Eqs. (27) and (28).

$$\boldsymbol{F}_{act,tot,i} = \begin{cases} \sum_{k=1}^{3}\left(\boldsymbol{F}_{act,i,1,k} + \boldsymbol{F}_{act,i,2,k}\right) & 1 \le i \le 3 \\ \sum_{k=1}^{3}\boldsymbol{F}_{act,i,2,k} & 4 \le i \le 6 \end{cases} \tag{27}$$

$$\boldsymbol{M}_{act,tot,i} = \begin{cases} \sum_{k=1}^{3}\begin{bmatrix} \left(\boldsymbol{p}_{hl,i,1,k} - \boldsymbol{p}_{jnt,i}\right)\times\boldsymbol{F}_{act,i,1,k} \\ +\left(\boldsymbol{p}_{hl,i,2,k} - \boldsymbol{p}_{jnt,i}\right)\times\boldsymbol{F}_{act,i,2,k} \end{bmatrix} & 1 \le i \le 3 \\ \sum_{k=1}^{3}\left(\boldsymbol{p}_{hl,i,2,k} - \boldsymbol{p}_{jnt,i}\right)\times\boldsymbol{F}_{act,i,2,k} & 4 \le i \le 6 \end{cases} \tag{28}$$

4 NUMERICAL IMPLEMENTATION

This section discusses the numerical implementation of the kinematic and statics models in MATLAB.

4.1 Kinematic Model MATLAB Implementation

A two-stage solver is used to solve the uniform-curvature kinematic model defined in Section 3.3.

In the first stage, only the segment 1 joint angles (β_A and γ_A) and governing equations ($L_{cbl,1,k,des} - L_{cbl,1,k} = 0$) are considered. Because the two calculated cable lengths $L_{cbl,1,k}$ are defined only by β_A and γ_A and $L_{cbl,1,k,des}$ is prescribed as an input, the two segment 1 joint angles may be solved for independent of β_B and γ_B. MATLAB's 'fsolve' function is used to solve for β_A and γ_A by iteratively driving the difference between the desired and calculated cable lengths to zero through modifications to the two angle inputs.

In the second stage, the calculated values of β_A and γ_A are set as constants in the solver, and a similar process using 'fsolve' is performed to iteratively calculate β_B and γ_B using the second pair of governing equations in Eq. (9).

4.2 Statics Model MATLAB Implementation

As with the kinematic model, 'fsolve' was used to find an acceptable set of the 16 DOF that would result in static equilibrium in the 12 joints (Eq. (10)) and valid compatibility conditions (Eq. (9)).

Two challenges arose when implementing the statics model described in Section 3.4: (1) how to enforce the joint angle limits; and (2) how to change the tensioned cables during simulation.

To address challenge (1), three approaches were considered for implementing the joint angle limits: (a) include a high-stiffness non-linear spring in the model that would engage when a joint angle exceeded ±35°, or (b) utilize a numerical solver that allows joint angle limits to be specified, or (c) DOF reduction (when a DOF is driven past its joint angle, it is removed from the optimization and replaced by the upper or lower limit in subsequent calculations).

Approach (a) was attempted, but led to convergence issues due to the highly nonlinear behavior of the spring. Approach (b) was undesirable, because the convergence properties of the 'fsolve' algorithm are superior to any built-in MATLAB functions that allow for upper and lower bounds on the DOF vector. Therefore, approach (c) was implemented.

Using this approach, for the first iteration, the statics of the robot are calculated like normal. Then, the output vector is evaluated to see if any joint angles exceed the upper or lower bounds. As soon as one does, it is removed from the DOF vector, its value is fixed at the upper or lower bound, and the simulation is re-run with one fewer DOF. This process is repeated until all joint angle elements of the DOF vector fit within the upper and lower joint angle bounds.

Challenge (2) arises because for some values of spring stiffness and the distributed mass, the cables that would tension a set of cable lengths for the shape resulting in a purely kinematic model (the initial guess for the static solver solution) do not necessarily actuate the final solution. As a result, in some cases, negative tensions were calculated in cables, which is not possible.

To address challenge (2), instead of utilizing the four tensions as the DOF, two magnitude/angle pairs (M_j and ϕ_j) are used to specify the actuation for the cables terminating in segments j = 1,2. The magnitude M_j represents the magnitude of the moment generated by the mutual action of the one or two non-zero tensions, and the angle ϕ_j represents the angle of rotation of the moment axis.

The angle ϕ_j controls which cables will have non-zero tensions, as shown in Table 2.

Table 2. Non-zero cable tensions due to ϕ_j

Angle	Non-Zero Tension	Angle	Non-Zero Tension
0°	Cable 1	(0°,120°)	Cables 1 and 2
120°	Cable 2	(120°,240°)	Cables 2 and 3
240°	Cable 3	(240°,360°)	Cables 3 and 1

For cases in which only one cable tension is non-zero, the cable tension can be calculated by dividing M_j by r_h.

For cases in which there are two non-zero tensions, the tensions are calculated by taking the sum of the cross products of $\boldsymbol{p}_{hl,j,k,lcl}$ (the local hole position vector) and [0, 0, $T_{j,k}$] for the two non-zero tensions and equate this to M_j [sin ϕ_j, cos ϕ_j, 0].

This will result in two non-trivial equations that can be used to solve for the two non-zero tensions for each segment.

5 RESULTS

This section analyzes the impact of actuation, elastic and gravitational effects on the accuracy of the purely kinematic model as a substitute for the static model.

Table 3 provides the baseline parameters used for the numerical simulations. In the following simulations, these parameters will be used unless specifically overridden.

Table 3. Tail simulation parameters

Variable	Value	Variable	Value
$L_{dsk2jnt}$	40 (mm)	$L_{jnt2dsk}$	40 (mm)
$L_{COM,dsk,\{1\text{-}5\}}$	0 (mm)	$L_{COM,dsk,6}$	8.45 (mm)
r_h	34 (mm)	r_{sp}	5.94 (mm)
$d_{sp,jnt}$	5.77 (mm)	$d_{sp,dsk}$	4.77 (mm)
$m_{dsk,whl}$	58.3 (g)	$m_{dsk,hlf}$	44.35 (g)
m_{jnt}	10.91 (g)	$L_{sp,0}$	25.4 (mm)
$k_{sp,\{1\text{-}3\}}$	7500 (N)	$k_{sp,\{4\text{-}6\}}$	2500 (N)
$F_{sp,pre,\{1\text{-}3\}}$	0 (N)	$F_{sp,pre,\{4\text{-}6\}}$	0 (N)

5.1 Actuation Effects

Figure 3 compares the kinematic and static model configurations for various sets of desired cable lengths leading to parallel bending of segments 1 and 2. The cable displacements were calculated varying the angle in each β-joint from 0° to 30° in 5° increments. Given this method of

determining the desired cable lengths, the kinematic model results in tail configurations with uniform joint angles along the length, with the straight configuration correlating to the $\beta_i = 0^o$ case and the half-circle configuration correlating to the $\beta_i = 30^o$ case .

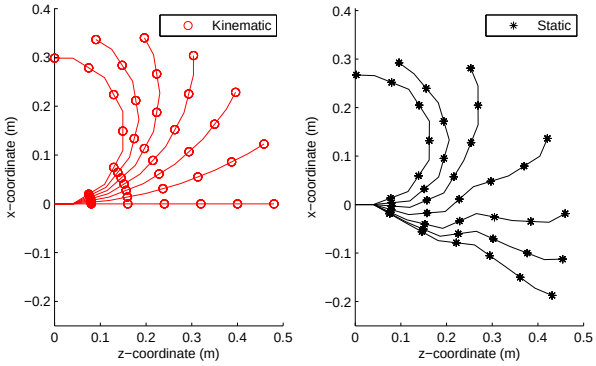

Figure 3. Comparison of configurations from kinematic and statics models for cooperative segment bending.

Due to the interaction between the gravitational and elastic effects, the static configuration correlating to the $\beta_i = 0^o$ kinematic model case exhibits significant 'sag'. If the springs were infinitely rigid, the static and kinematic cases would be equivalent. However, because the joints must deflect to generate an elastic moment to counter the gravitational moment, the static model sags.

However, unlike a conventional cantilevered beam, the joint angles are not all of the same sign in this configuration due to the prescribed cable displacements. In the kinematic case for $\beta_i = 0^o$, the total segment joint angle in each of the two segments is 0^o. Therefore, the sum of these joint angles in the static case should also approximate zero (the cable displacements due to positive vs negative joint angle are not precisely equal and opposite). Therefore, in the first segment, because the gravitational loading is greatest on joint β_1, it will be negative. And because the segment 1 actuation loading is applied primarily on joint 3, β_3 is positive.

However, as the cable displacements increase, the static model configuration more and more closely resembles the kinematic configuration. This is due to two factors: (1) reduction of gravitational moment, and (2) joint angle constraints.

The reduction of the gravitational moment begins to occur after the third shown configuration (kinematic $\beta_i = 10^o$). In this case, the tail is almost fully extended (albeit slight sagging in the two segments). However, in the subsequent configuration (kinematic $\beta_i = 15^o$) the center of mass of the tail has moved toward the base instead of away. As the tail continues increasing its curvature, this continues, reducing the gravitational moment.

In addition, the joint angle stops aid in transmitting internal loading along the tail. When a joint is not at its limit, the joint's internal moment is required to be zero by static equilibrium. However, when at a joint limit, this is not true.

Beyond simply analyzing the configurations, Figure 4 illustrates the cable 1-1 tension associated with each static configuration. The cable tension provides the loading to overcome the net effect of the gravitational and elastic loading. As shown, the tension increase until the kinematic $\beta_i = 15^o$, then suddenly decreases. In Fig. 3, between $\beta_i = 15^o$ and 20^o, the tail tip bends back over the tail. When this happens, the disk 6 gravitational force begins to aid in the subsegment 6 bending instead of opposing it. This reduces the loading on the actuation to maintain the desired configuration, resulting in a reduced cable tension.

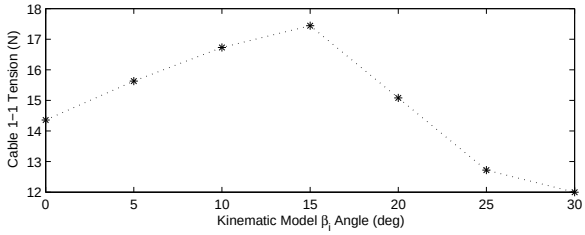

Figure 4. Cable 1-1 tension profile for parallel actuation.

The profiles for cables 2-2 and 2-3 are similar in shape, but differ in magnitude. For example, for the kinematic $\beta_i = 0^o$ case, the cable 1-1 tension is 14.36 N, but the cable 2-2 and 2-3 tensions are 1.89. The order of magnitude difference between these values is because segment 1's actuation supports the mass of segments 1 and 2 through the internal force transmitted from joint to joint, whereas segment 2's actuation only supports the mass in segment 2. However, the trade-off is that the second segment cables are subject to greater displacements, because the cables pass through six subsegments instead of three.

Figure 5 compares the kinematic and static model configurations for antagonistic bending of segments 1 and 2. The $\beta_{1\text{-}3}$ angles are the same in this simulation as the parallel configuration simulations in Fig. 3, and the $\beta_{4\text{-}6}$ angles are equal and opposite to the values for the simulations in Fig. 3.

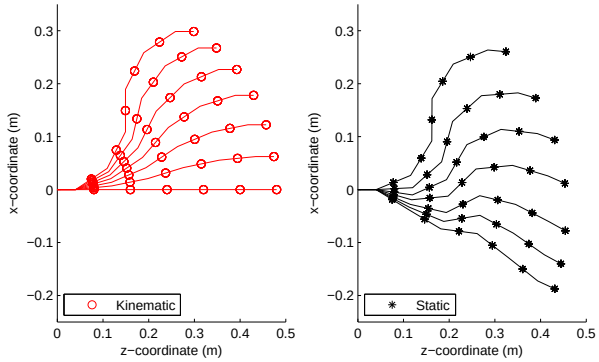

Figure 5. Comparison of configurations from kinematic and statics models for antagonistic segment bending.

A similar pattern is seen for this set of simulations and those in Fig. 3, where the low-actuation static cases exhibit significant sag and variation from the kinematic model, but

become more accurate as actuation increases. However, even at lower actuations, because the second segment's desired bending is the same direction as the bending due to gravity, the accuracy is improved further still.

During these simulations, a change in the cables tensioned is also observed in the second segment. Figure 6 illustrates the segment 2 cable tensions. Between $\beta_{1\text{-}3} = 10^o$ and 15^o, cables 2-2 and 2-3 transition to zero tension and cable 2-1 engages. For $\beta_{1\text{-}3} = 10^o$ and below, the actuation was primarily acting against gravity to hold the tail configuration. However, for $\beta_{1\text{-}3} = 15^o$ and above, the actuation is primarily acting against the segment elasticity.

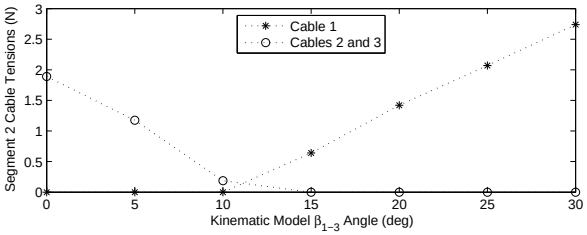

Figure 6. Segment 2 cable tensions for antagonistic actuation loading.

5.2 Elastic Effects

Figure 7 shows the impact of spring stiffness on the tail configuration. For the segment 1 variation, the spring stiffness was varied from 4500 N/m to 16500 N/m in 3000 N/m increments, and for the segment 2 variation, the spring stiffness was varied from 1000 N/m to 7000 N/m in 1500 N/m increments. Cable displacements match the $\beta_i = 0^o$ case in Fig. 3.

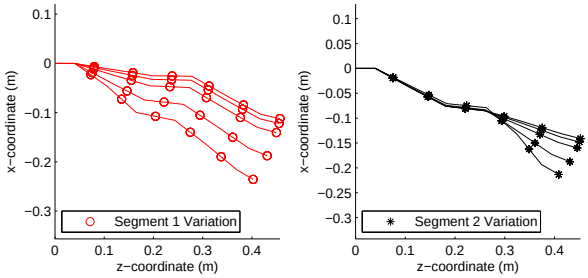

Figure 7. Change in zero-displacement configurations due to spring stiffness variation in segments 1 and 2.

In each case, as the stiffness is increased, as expected, the static result becomes more straight. However, the marginal benefit of increase the stiffness decreases as the stiffness increases. Although not the focus of the analysis at this stage, the downside to increasing the spring stiffness is that it will reduce the tail's maximum accelerations for a prescribed cable displacement, thereby reducing its inertial loading capability.

Furthermore, in the second segment, increasing the stiffness also tends to increase the gravitational moment loading on segment 1, thereby increasing β_1 and further sagging the tail.

5.3 Gravitational Effects

Figure 8 shows two sets of simulations for different modifications for the subsegment mass. $\beta_i = 45^o$ case in Fig. 3. In the left frame, the mass of each disk assembly (both whole and half) was increased by the same amount, correlating to an increase in the mass of the disk. In the right frame, additional mass was only provided at the half disk-assembly (i.e., disk 6) at the tail tip. For the distributed mass, the amount added to each disk varied from 0 g to 20 g , in 5 g increments (total added mass varied from 0 g to 120 g in 30 g increments). For the tip mass, the amount added to disk 6 varied from 0 g to 100 g in 25 g increments.

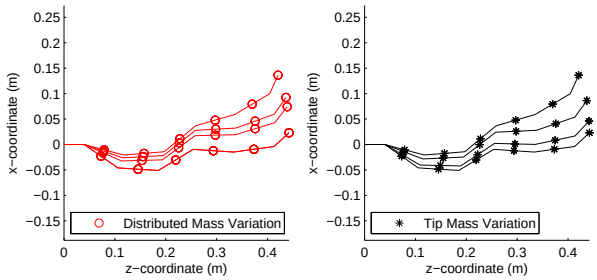

Figure 8. Change in configurations due to tail mass variation (a) distributed along length and (b) at tip.

As shown, the marginal effects of adding the given distributed mass or tip mass are the same, despite the difference in the total amount added.

However, in each case, each simulation converges to the same final configuration, due to the joint limits. In the extreme cases (20g x 6 disks, or 100 g at the tip), joints 1 and 4 are both -35^o and joints 3 and 6 are both 35^o. In each segment, this leaves one DOF for joint 2 or 5, and one DOF for the cable tension. Therefore, because the cable length constraint only incorporates the joint angles, in segment 1, the joint 2 angle is analytically calculable because joints 1 and 3 are known, and the cable tension can be calculated from the single static equilibrium equation. This is also true for segment 2. Therefore, once four joint angle limits are reached, the only modification effected by adding more mass is to increase the cable tensions.

6 CONCLUSION

This paper presented kinematic and static models for a serpentine tail structure capable of calculating the resulting joint angles (both models) and cable tension (static model) given a prescribed set of desired actuation cable displacements. Simulations were generated to analyze the impact of actuation, elastic and gravitational effects on the tail configuration and cable tensions, including the correlation between the kinematic and static models.

Future work will incorporate inertial effects into the static model to make it a dynamic model, and will use this model to aid in the design of a serpentine tail for use on-board a mobile robot to aid in maneuvering and stabilization. The prototypes

resulting from these designs will be used in part to experimentally validate this and future associated work.

ACKNOWLEDGMENTS

This material is based upon work supported by the National Science Foundation under Grant No. 1334227.

REFERENCES

[1] Kopman, V., Laut, J., Acquaviva, F., Rizzo, A., and Porfiri, M., 2014, "Dynamic Modeling of a Robotic Fish Propelled by a Compliant Tail," IEEE J. Ocean. Eng., **40**(1), pp. 209–221.

[2] Wright, C., Buchan, A., Brown, B., Geist, J., Schwerin, M., Rollinson, D., Tesch, M., and Choset, H., 2012, "Design and Architecture of the Unified Modular Snake Robot," IEEE International Conference on Robotics and Automation, St. Paul, MN, pp. 4347–4354.

[3] Liu, G.-H., Lin, H.-Y., Lin, H.-Y., Chen, S.-T., and Lin, P.-C., 2013, "Design of a Kangaroo Robot with Dynamic Jogging Locomotion," IEEE/SICE International Symposium on System Integration, Kobe, Japan, pp. 306–311.

[4] Zhao, J., Zhao, T., Xi, N., Cintron, F. J., Mutka, M. W., and Xiao, L., 2013, "Controlling Aerial Maneuvering of a Miniature Jumping Robot Using Its Tail," IEEE/RSJ International Conference on Intelligent Robots and Systems, Tokyo, Japan, pp. 3802–3807.

[5] Kohut, N. J., Haldane, D. W., Zarrouk, D., and Fearing, R. S., 2012, "Effect of Inertial Tail on Yaw Rate of 45 Gram Legged Robot," Int. Conf. Climbing Walk. Robot. Support Technol. Mob. Mach., pp. 157–164.

[6] 2002, "One Small Step for Dinosaurs...TROODY the robotic dinosaur walks the walk" [Online]. Available: http://web.mit.edu/spotlight/archives/troody.html.

[7] Patel, A., and Braae, M., 2013, "Rapid Turning at High-Speed: Inspirations from the Cheetah's Tail," IEEE/RSJ International Conference on Intelligent Robots and Systems, Tokyo, Japan, pp. 5506–5511.

[8] Patel, A., and Braae, M., 2014, "Rapid Acceleration and Braking: Inspiration from the Cheetah's Tail," IEEE International Conference on Robotics and Automation, pp. 793–799.

[9] Mao, Y., and Agrawal, S. K., 2012, "Design of a Cable-Driven Arm Exoskeleton (CAREX) for Neural Rehabilitation," IEEE Trans. Robot., **28**(4), pp. 922–931.

[10] Mustafa, S. K., and Agrawal, S. K., 2012, "On the Force-Closure Analysis of n-DOF Cable-Driven Open Chains Based on Reciprocal Screw Theory," IEEE Trans. Robot., **28**(1), pp. 22–31.

[11] Boyle, J. H., Johnson, S., and Dehghani-Sanij, A. A., 2013, "Adaptive Undulatory Locomotion of a C. elegans Inspired Robot," IEEE/ASME Trans. Mechatronics, **18**(2), pp. 439–448.

[12] Maity, A., and Majumder, S., 2011, "Serpentine Robots: A Study of Design Philosophy," IEEE International Conference on Advanced Robotics, Tallinn, Estonia, pp. 549–555.

[13] Kim, Y. J., Cheng, S., Kim, S., and Iagnemma, K., 2014, "A Stiffness-Adjustable Hyperredundant Manipulator Using a Variable Neutral-Line Mechanism for Minimally Invasive Surgery," IEEE Trans. Robot., **30**(2), pp. 382–395.

[14] Kwok, K. W., Mylonas, G. P., Sun, L. W., Lerotic, M., Clark, J., Athanasiou, T., Darzi, A., and Yang, G. Z., 2009, "Dynamic Active Constraints for Hyper-Redundant Flexible Robots," Medical Image Computing and Comptuer-Assisted Intervention, Springer Berlin Heidelberg, pp. 410–417.

[15] OC-Robotics, 2015, "Snake-Arm Robots" [Online]. Available: http://www.ocrobotics.com/technology--innovation/. [Accessed: 20-Jan-2015].

[16] Chang-Siu, E., Libby, T., Tomizuka, M., and Full, R. J., 2011, "A Lizard-inspired Active Tail Enables Rapid Maneuvers and Dynamic Stabilization in a Terrestrial Robot," 2011 IEEE/RSJ International Conference on Intelligent Robots and Systems, San Francisco, CA, pp. 1887–1894.

[17] Berenguer, F. J., and Monasterio-Huelin, F. M., 2008, "Zappa, a Quasi-Passive Biped Walking Robot With a Tail: Modeling , Behavior , and Kinematic Estimation Using Accelerometers," IEEE Trans. Ind. Electron., **55**(9), pp. 3281–3289.

[18] Rone, W. S., and Ben-Tzvi, P., 2014, "Continuum Robot Dynamics Utilizing the Principle of Virtual Power," IEEE Trans. Robot., **30**(1), pp. 275–287.